



Article

## MOF-derived Co-Fe bimetallic oxygen reduction electrocatalysts for alkaline fuel cells

Yin Xiong, Yao Yang, Francis J. DiSalvo, and Héctor D. Abruña

*J. Am. Chem. Soc.*, Just Accepted Manuscript • DOI: 10.1021/jacs.9b03561 • Publication Date (Web): 19 Jun 2019

Downloaded from <http://pubs.acs.org> on June 25, 2019

### Just Accepted

“Just Accepted” manuscripts have been peer-reviewed and accepted for publication. They are posted online prior to technical editing, formatting for publication and author proofing. The American Chemical Society provides “Just Accepted” as a service to the research community to expedite the dissemination of scientific material as soon as possible after acceptance. “Just Accepted” manuscripts appear in full in PDF format accompanied by an HTML abstract. “Just Accepted” manuscripts have been fully peer reviewed, but should not be considered the official version of record. They are citable by the Digital Object Identifier (DOI®). “Just Accepted” is an optional service offered to authors. Therefore, the “Just Accepted” Web site may not include all articles that will be published in the journal. After a manuscript is technically edited and formatted, it will be removed from the “Just Accepted” Web site and published as an ASAP article. Note that technical editing may introduce minor changes to the manuscript text and/or graphics which could affect content, and all legal disclaimers and ethical guidelines that apply to the journal pertain. ACS cannot be held responsible for errors or consequences arising from the use of information contained in these “Just Accepted” manuscripts.

# MOF-derived Co-Fe bimetallic oxygen reduction electrocatalysts for alkaline fuel cells

Yin Xiong,<sup>†</sup> Yao Yang,<sup>†</sup> Francis J. DiSalvo, and Héctor D. Abruña\*

Department of Chemistry and Chemical Biology, Baker Laboratory, Cornell University, Ithaca, New York 14853, United States

Supporting Information Placeholder

**ABSTRACT:** The oxygen reduction reaction (ORR) is considered the cornerstone for regenerative energy conversion devices involving fuel cells and electrolyzers. The development of non-precious-metal electrocatalysts is of paramount importance for their large-scale commercialization. Here, Co-Fe binary alloy embedded bimetallic organic frameworks (BMOFs) based on carbon nanocomposites have been designed with a compositionally optimized template, by a facile host-guest strategy, for the ORR in alkaline media. The electrocatalyst exhibits promising electrocatalytic activity for the ORR with a half-wave potential of 0.89 V in 0.1 M NaOH; comparable to state-of-the-art Pt/C electrocatalysts. More importantly, it exhibits robust durability after 30,000 potential cycles. Scanning transmission electron microscopy (STEM) and quantitative energy-dispersive X-ray (EDX) spectroscopy suggest that the Co-Fe alloy nanoparticles have a homogenous elemental distribution of Co and Fe at the atomic-scale optimized BMOF and Co/Fe ratio of 9:1. The long-term durability is attributed to its ability to maintain its structural and compositional integrity after the cycling process, as evidenced by STEM-EDX analysis. This work provides valuable insights into the design and fabrication of novel PGM-free highly active ORR electrocatalysts in alkaline media.

## Introduction

The continuing consumption of non-renewable fossil fuels and increased aspiration for a global sustainable energy technology landscape, has stimulated the development of novel fuel cell technologies.<sup>(1)-(2)</sup> The regenerative energy conversion concept, targeting low-carbon or carbon-free fuels, makes it a promising approach to lower CO<sub>2</sub> emissions.<sup>3-4</sup> The challenge to accelerate the sluggish oxygen reduction reaction (ORR) at the cathode in fuel cell applications, will require novel materials and architectures. Platinum-group-metals (PGM) based materials are still considered to be the state-of-the-art electrocatalysts towards the ORR.<sup>5-7</sup> However, their large-scale application in fuel cells is still precluded by cost and limited stability.<sup>8-9</sup> Thus, there is a clear need to design and develop cost effective alternatives with high electrocatalytic activity and robust long-term stability. Alkaline polymer electrolyte fuel cells (APEFCs) have attracted a great deal of interest in the recent past because they can enable the use of non-precious metals as electrocatalysts for the ORR.<sup>10</sup> In this context, extensive investigations have focused on non-PGM materials, including transition metal oxide<sup>11-18</sup>, ranging from monometallic to trimetallic oxides, and PGM-free nitrogen doped carbon materials.<sup>19-21</sup> Dai and co-workers have reported on Mn-Co oxides loaded on N-doped reduced graphene oxide, which significantly enhanced the electrocatalytic activity by the covalent coupling effect between the support and the oxide nanoparticles.<sup>22</sup> Yang et al. studied perovskite-based oxides, applying them for both oxygen reduction and evolution reactions.<sup>23</sup> Zelenay and Dodelet have utilized nitrogen-containing organic molecules incorporating earth-abundant Co or Fe, to prepare metal-nitrogen-carbon (M-N-C) materials through high-temperature pyrolysis. The resulting materials have exhibited promising performance in membrane electrode assemblies (MEAs), providing further impetus to the industrial application of PGM-free electrocatalyst materials.<sup>24-27</sup> Furthermore, Lu et al., Peng et al. and Sa et al. have fabricated a

variety of non-PGM catalysts, including carbonaceous material derived from halloysite, CoO<sub>x</sub> nanohybrids and Fe, N doped carbon materials, respectively. They are adapted in APEFCs, and demonstrated excellent performance.<sup>28-30</sup>

Recently, metal organic frameworks (MOFs), (containing metal centers and organic linkers), have generated a great deal of attention as scaffolds and precursors for novel families of carbon nanocomposites.<sup>31-32</sup> As representatives of MOFs, zeolitic imidazolate frameworks (ZIFs) such as ZIF-67 and ZIF-8, with available metal centers and highly abundant carbon and nitrogen, have emerged as promising precursors as electrocatalysts.<sup>33-34</sup> The nitrogen species can bond to non-noble-metal nanoparticles as a means to yield N-doped carbon materials.<sup>35</sup> Nitrogen atoms can generate positively charged sites that are conducive to O<sub>2</sub> adsorption or splitting, which is believed to help expedite the kinetics of the oxygen reduction reaction.<sup>36-37</sup> There have been numerous reports on these context. Lou et al. employed ZIF-67 to produce porous hollow carbon polyhedra, comprised of N-doped carbon nanotubes (CNTs), as bifunctional electrocatalysts towards the ORR and OER.<sup>38</sup> Song et al. used ZIF-8 as a sacrificial framework that was pyrolyzed and activated with NH<sub>3</sub> for optimized N configuration/doping to boost electrocatalytic activity.<sup>39</sup> ZIF-67-derived materials feature N-doped mesoporous graphitic carbon with a stable structure, as well as high electronic conductivity and Co decoration for the generation of active sites. ZIF-8 provides a hollow framework with high surface area, promoting rapid diffusion kinetics during electrocatalysis. Jiang and coworkers, Su and coworkers and others, have employed bimetallic mixtures of ZIF-67 and ZIF-8 as templates, further doped with phosphate anions, to fabricate electrocatalytically active nanocarbon materials after pyrolysis in Ar.<sup>40-41</sup>

Herein, we report on a group of optimized bimetallic MOFs (BMOFs) derived from a Co-Fe alloy embedded in a carbon nanocomposite, which when compositionally optimized, exhibit

highly stable electrocatalytic activity towards the ORR. In ZIF-8, volatile

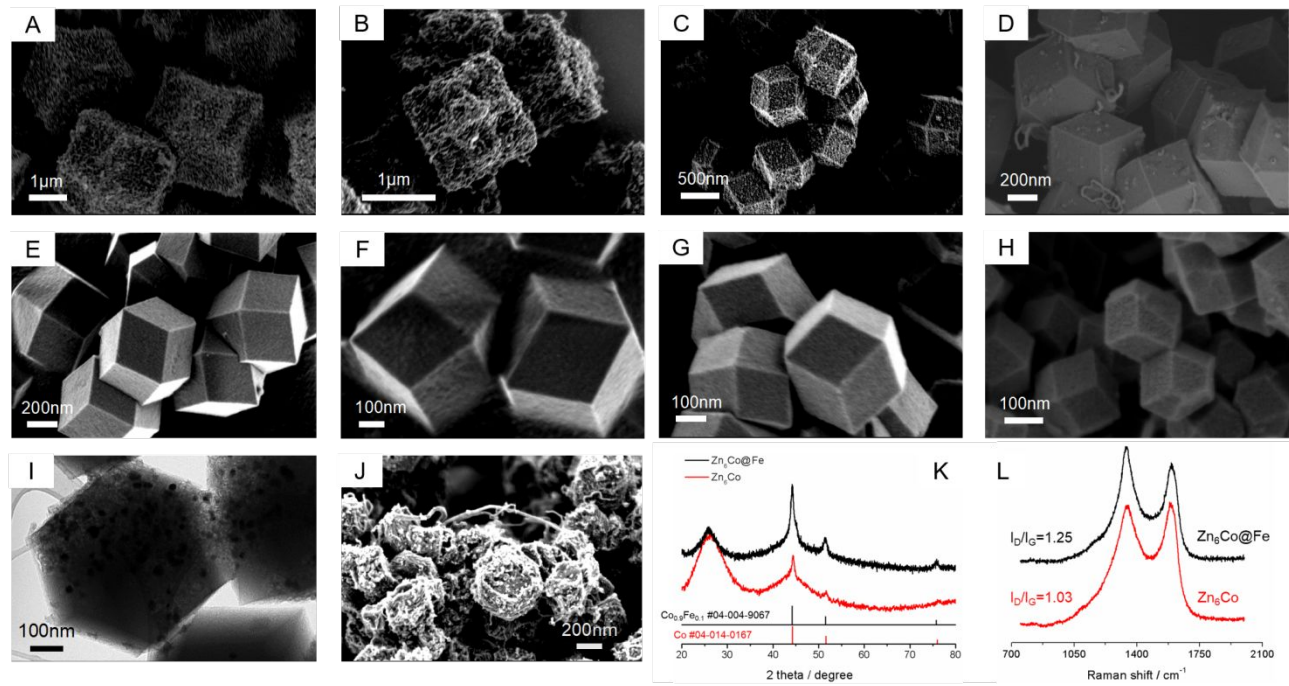


Figure 1. (A-H) SEM images of pyrolyzed BMOF\_Co, BMOF\_ZnCo<sub>3</sub>, BMOF\_ZnCo, BMOF\_Zn<sub>3</sub>Co, BMOF\_Zn<sub>6</sub>Co, BMOF\_Zn<sub>11</sub>Co, BMOF\_Zn<sub>20</sub>Co and BMOF\_Zn at 800°C in forming gas (95% N<sub>2</sub> and 5% H<sub>2</sub>) (I) TEM image of the pyrolyzed Zn<sub>6</sub>Co (J) SEM image of the pyrolyzed Zn<sub>6</sub>Co\_Fe (K) XRD patterns of Zn<sub>6</sub>Co and Zn<sub>6</sub>Co\_Fe (L) Raman spectrum of Zn<sub>6</sub>Co and Zn<sub>6</sub>Co\_Fe

Zn metal centers can evaporate, generating a carbon structure with high surface area and porosity. The resulting cavities served as hosts to encapsulate Fe ions to form a Co-Fe alloy with cobalt derived from the ZIF-67 or with externally added Fe(acac)<sub>3</sub>. The resulting nanocomposite exhibited ORR electrocatalytic activity comparable to commercial Pt, as well as high stability for the ORR in alkaline media as evidenced by its compositional and structural integrity.

## Results and discussion

A family of Co-Zn bimetallic MOFs (BMOFs) precursors were synthesized by a facile one-step solvothermal method at room temperature, through the self-assembly of Co<sup>2+</sup>/Zn<sup>2+</sup> with 1/2-methyimidazole in a solvent mixture of ethanol and methanol. Their compositions were varied systematically and labeled as BMOF-Co, ZnCo<sub>3</sub>, ZnCo, Zn<sub>3</sub>Co, Zn<sub>6</sub>Co, Zn<sub>11</sub>Co, Zn<sub>20</sub>Co and Zn, representing the fraction of the Co<sup>2+</sup> salt (Co(NO<sub>3</sub>)<sub>2</sub>) as 100%, 75%, 50%, 14%, 8%, 5% and 0%, respectively. The powder X-ray diffraction (XRD) patterns of the resulting BMOFs are shown in Figure S1, where those of BMOF\_Co and Zn were consistent with the simulated XRD patterns of ZIF-67 and ZIF-8, respectively. The intermediate XRD patterns, were analogous to ZIF-67 and ZIF-8, indicating the successful synthesis of the BMOFs. Their morphologies were characterized via scanning electron microscopy (SEM) and transmission electron microscopy (TEM), shown in Figure S2 and Figure S3, indicating a uniform distribution and smooth surfaces. The BMOF crystal sizes decreased at higher Zn/Co ratios in the metal precursors with less metallic Co nanoparticles remained. The crystal size decreased from the BMOF-Co sample, with an average edge length of around 2 μm, to around 1 μm in BMOF\_ZnCo, and eventually to <100 nm in BMOF\_Zn. As expected, there exists a correlation between the diminution in the crystal size and the increasing fraction of Co in the salt precursors. The formed polyhedra were pyrolyzed under

forming gas at 800°C for 2 h, followed by a sulfuric acid wash to remove any leachable metallic Co. As shown in Figure 1A-H, the polyhedral morphology of the crystals was retained after the heat-treatment and acid wash. It is generally accepted that CNTs (carbon nanotubes) would likely grow on most transition metals at elevated temperatures and under a sufficiently high H<sub>2</sub> pressure.<sup>42</sup> The nanocomposites with higher Co content yielded rougher surfaces, suggesting the formation of a higher amount of carbon nanotubes. Figure S4 shows the XRD patterns of the carbonized BMOFs, in which all materials exhibited two peaks at 25° and 44° indexed to the (002) and (101) peaks of carbon, and XRD peaks at 44° and 51° ascribed to the (111) and (200) peaks of metallic Co in a face-centered cubic structure. At higher Co contents, metallic Co peaks became more pronounced. The generated Zn oxide was expected to be reduced in the forming gas atmosphere or by carbon, which subsequently vaporized at high temperature. Thus, there were no diffraction peaks from Zn. The TGA measurements in Figure S5A were used to confirm the complete removal of Zn. The residual mass of pyrolyzed BMOFs was precisely proportional to the amount of Co precursors, and the Co-free material had nearly a 100% mass loss after acid leaching. The BMOF material derived from the Zn<sub>6</sub>Co composite, was further used as the scaffold to encapsulate the Fe<sup>3+</sup> in its cavities/pores via the double solvent method.<sup>43-44</sup> The Fe<sup>3+</sup> moieties were immobilized in the pores of the Zn<sub>6</sub>Co network and reduced simultaneously with their neighboring Co atoms, creating the bimetallic active sites after carbonization and acid leaching.

Figures S6A-B show the morphology of BMOF\_Zn<sub>6</sub>Co before and after thermal treatment and acid leaching, confirming that neither of the two processes affected the overall morphology. The TEM image of the pyrolyzed BMOF\_Zn<sub>6</sub>Co in Figure 1I demonstrates that the polyhedral scaffold of carbon was embedded with metallic Co nanoparticles. With the incorporation of Fe, the resulting carbon nanocomposite, derived from Zn<sub>6</sub>Co (labeled as

**Zn<sub>6</sub>Co-Fe**), had abundant carbon nanotubes, covering the surface of the polyhedral crystals (**Figure 1J**). The XRD patterns of pyrolyzed Zn<sub>6</sub>Co and Zn<sub>6</sub>Co-Fe revealed that, metallic Co and bimetallic Co<sub>0.9</sub>Fe<sub>0.1</sub> were formed in the reducing atmosphere during carbonization and were retained after the acid wash. The diffraction pattern of the pyrolyzed Zn<sub>6</sub>Co-Fe in **Figure 1K**, exhibited a slight shift to lower angles compared with the non-Fe counterpart, consistent with the larger atomic radius of Fe. There were two peaks observed in the Raman spectrum shown in **Figure 1L**, illustrating the D and G band features of carbon. The Raman peaks located at 1350 and 1600 cm<sup>-1</sup> were attributed to sp<sup>2</sup> graphitic and defects in the carbon, respectively.

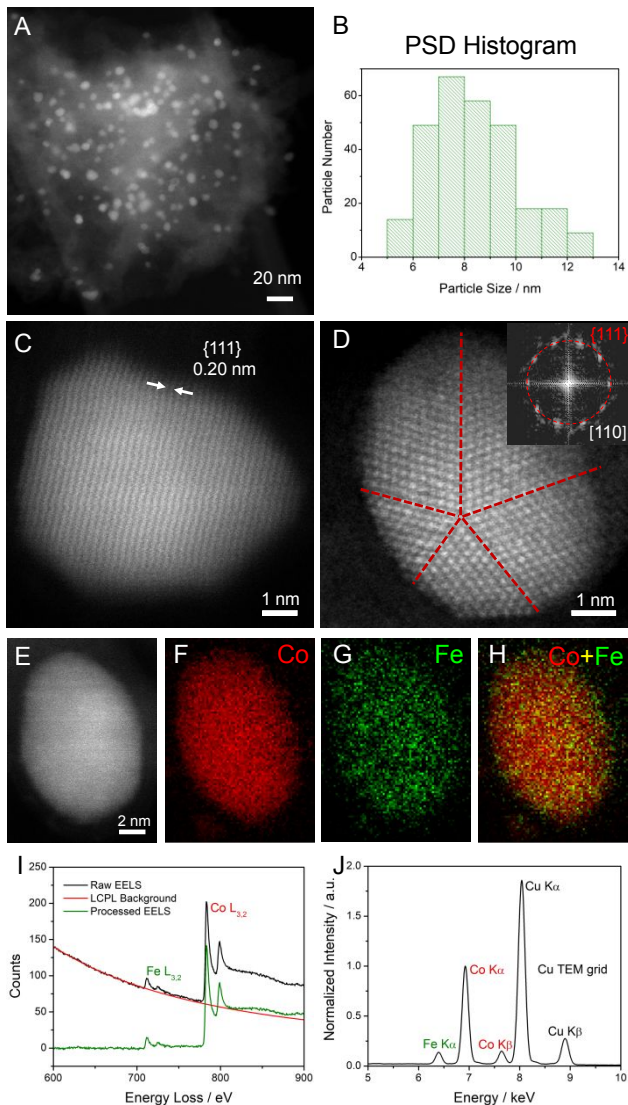


**Figure 2.** HAADF-STEM images of Co<sub>0.9</sub>Fe<sub>0.1</sub> bimetallic nanoparticles embedded in a MOF-derived porous carbon matrix (BMOF). (A) low-magnification STEM image of BMOF (B) particle size distribution (PSD) histogram of about 300 particles analyzed from (A) and Figure S4. (C) Atomic-scale STEM image of a single crystal with a d-spacing value of 0.20 nm, indicating {111} facets of Co<sub>0.9</sub>Fe<sub>0.1</sub>. (D) Atomic-scale STEM image of a nanoparticle with five sub-domains on the [110] zone axis and the domain boundaries indicated as the red dashed lines. Inset shows the corresponding Fourier transform with five pairs of {111} diffraction spots; Chemical composition of a Co<sub>0.9</sub>Fe<sub>0.1</sub> bimetallic nanoparticle. (E-H) STEM image and the corresponding EELS elemental maps of Co (red), Fe (green) and the composite map (Co

vs. Fe). (I) Processed EELS spectrum with pronounced Fe and Co L<sub>3,2</sub> edges (J) STEM-EDX spectrum with Fe K $\alpha$  and Co K $\alpha, \beta$  edges. Quantitative EDX analysis suggests Fe, Co contents of 89.2 at.% and 10.8 at.%, respectively.

The defects could come from the heteroatom substitution, vacancies, and grain boundaries, which are commonly considered to be more active in electrocatalysis than the basal plane.<sup>45</sup> The D/G band ratio increased from 1.03 to 1.25 following the addition of Fe, indicating the formation of more defect sites facilitating electrocatalysis. It was speculated that the volatile Zn would substantially increase the surface area. The BET surface areas of four representative samples, the carbon nanocomposites from Co, Zn<sub>6</sub>Co, Zn and Zn<sub>6</sub>Co-Fe were measured to be 520, 1310, 1400 and 745 m<sup>2</sup>/g, respectively. The high surface area allowed the exposure of active sites and was deemed beneficial to the rapid transport of O<sub>2</sub> and relevant species during the electrocatalysis processes (**Figure S5B**).

The atomic structure of the Co<sub>0.9</sub>Fe<sub>0.1</sub>, embedded in the carbon nanocomposite, derived from Zn<sub>6</sub>Co-Fe, was further examined by high-angle annular dark-field (HAADF) STEM imaging. Since STEM image intensity is proportional to the atomic number ( $I \propto Z^{1.7}$ ), the Co<sub>0.9</sub>Fe<sub>0.1</sub> alloy particles will be significantly brighter than the carbon support. As shown in **Figure 2A**, Co<sub>0.9</sub>Fe<sub>0.1</sub> bimetallic nanoparticles (NPs) were uniformly distributed and embedded in the MOF-derived porous carbon matrix. Co<sub>0.9</sub>Fe<sub>0.1</sub> NPs exhibited narrow particle size distribution (PSD) of  $8 \pm 2$  nm (average  $\pm$  one standard deviation, S<sub>d</sub>), (**Figure 2B**) based on an analysis of more than 300 nanoparticles from **Figures 2A** and S7. The crystal structure was further examined by STEM images at the atomic scale. **Figure 2C** shows a single-crystal nanoparticle with a d-spacing value of 0.20 nm, which is consistent with the theoretical radius of Co<sub>0.9</sub>Fe<sub>0.1</sub> {111} facets, 0.2048 nm (PDF # 04-004-9067). Another Co<sub>0.9</sub>Fe<sub>0.1</sub> nanoparticle was found to have five sub-domains of {111} d-spacings on the same zone axis of [110] (**Figures 2D** and S8). Domain boundaries were marked with red dashed lines, and the hexagonal symmetry of [110] in each domain was clearly resolved from the atom arrangements. The Fourier transform of this nanoparticle showed the corresponding five pairs of diffraction spots with the same d-spacing values, as indicated by the dashed red circle (**Figure 2D** inset). The energy loss spectroscopy (EELS) and energy-dispersive X-ray spectroscopy (EDX). **Figure 2I** shows the pronounced Co and Fe L<sub>3,2</sub> edges at around 790 and 710 eV, respectively, which were used to extract 2D EELS elemental mapping. **Figure 2E-F** presents a 10 nm Co<sub>0.9</sub>Fe<sub>0.1</sub> nanoparticle with EELS maps of Co (red) and Fe (green). The EELS composite map of Co vs. Fe in the upper right of **Figure 2E-F** suggested a relatively homogenous distribution of Co and Fe, which was further evidenced by similar EELS maps in **Figure S9**. This provides convincing and compelling evidence of the formation of a Co-Fe alloy at the atomic-scale, which is consistent with the observation from the XRD of Co<sub>0.9</sub>Fe<sub>0.1</sub> in **Figure 2K**. Besides the elemental distribution from EELS, EDX also served as a quantitative tool to analyze the local atomic ratio (**Figure 2J**). Co and Fe K $\alpha$  edges at 6.9 and 6.4 keV, respectively, were employed to calculate the relative atomic contents of Fe and Co, based on the Cliff-Lorimer equation.<sup>46</sup> Co and Fe were found to have relative contents of 89.2% and 10.8%, respectively, which is consistent with the designed stoichiometry of Co/Fe (9:1) and ICP-MS results, which indicated that the atomic ratio of Co to Fe was around 9:1. The relative error was defined as one S<sub>d</sub> of 0.6 %, based on a random selection of five different regions on the TEM grid. The strong Cu signal in **Figure 2J** came from the Cu TEM grid. STEM-EDX elemental maps of several Co<sub>0.9</sub>Fe<sub>0.1</sub> NPs also yielded a similar homogenous distribution of Co and Fe to that obtained from EELS mapping (**Figure S10**). In summary, microscopic-level STEM-EELS mapping, combined with quantitative EDX analysis,

unambiguously indicate that the  $\text{Co}_{0.9}\text{Fe}_{0.1}$  alloy nanoparticles have a homogenous distribution of Co and Fe at the atomic scale with the designed Co/Fe ratio of 9:1.

With the desirable structural information discussed above, the electrocatalytic performance of these materials, towards the ORR, was assessed in alkaline media. Shown in Figure 3A, all the polarization curves of all BMOFs derived carbon nanocomposites collected in a conventional three-electrode system at 1600 rpm, in an  $\text{O}_2$ -saturated 0.1M NaOH electrolyte, at a scan rate of 5 mV/s and a rotation rate of 1600 rpm. The mass activities at 0.85 V and the half-wave potentials are summarized in Figure 3B. The Zn-derived material showed the lowest onset potential and the slowest kinetics in the mixed diffusion-kinetics control region. In sharp contrast, with a minimal amount of Co incorporated, the electrocatalytic performance of the  $\text{Zn}_{20}\text{Co}$ -derived sample had a dramatically enhanced increase of 200% in mass activity, and a 30 mV positive shift in the half-wave potential. This dramatic improvement indicated that Co provided critical active sites for ORR electrocatalysis. With additional increases in the Co loading, there were further increases in the mass activity, although the additional relative enhancement gradually decreased with higher Co contents. Contrary to such behavior, in the case of  $\text{Zn}_6\text{Co}$  to Co, the electrocatalytic activity decreased in increasing levels of Co. As a result,  $\text{Zn}_6\text{Co}$  proved to be the best ORR candidate derived from BMOFs precursors. We ascribe this to its high surface area, accessible Co-based active sites and N dopants. Furthermore, the Co-Fe bimetallic alloy derived from  $\text{Zn}_6\text{Co}$ , namely  $\text{Zn}_6\text{Co}_\text{Fe}$ , exhibited an electrocatalytic activity that surpassed those of  $\text{Zn}_6\text{Co}$  and commercial Pt/C, in terms of the half-wave potential (Figure 3C).

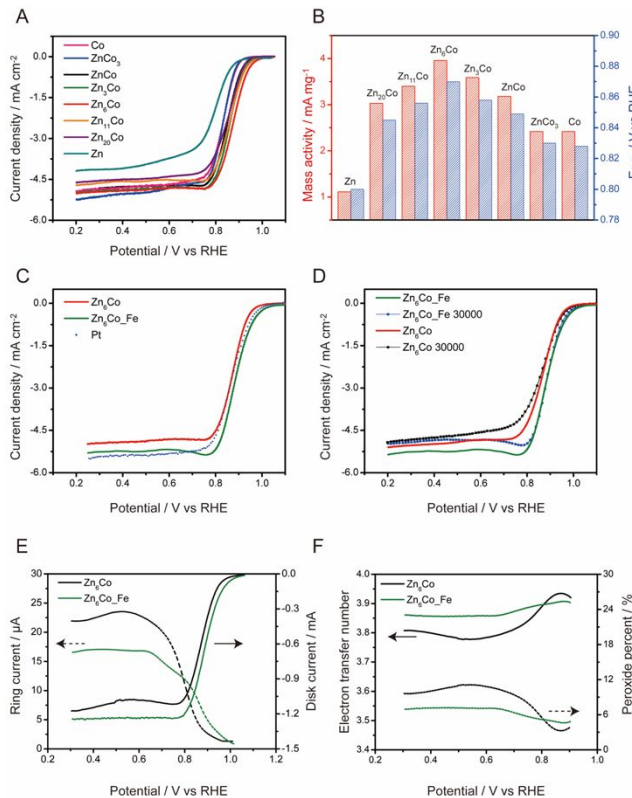


Figure 3. Oxygen reduction on pyrolyzed BMOFs and  $\text{Zn}_6\text{Co}_\text{Fe}$ . (A) Polarization curves of a variety of BMOFs samples obtained in  $\text{O}_2$ -saturated 0.1M NaOH at 1600 rpm and a scan rate of 5 mV/s. (B) Comparison of the mass activity at 0.85V and half wave potentials ( $E_{1/2}$ ). (C) Polarization curves of pyrolyzed  $\text{Zn}_6\text{Co}$ .

and  $\text{Zn}_6\text{Co}_\text{Fe}$  and commercial Pt. (D) Polarization curves of  $\text{Zn}_6\text{Co}$  and  $\text{Zn}_6\text{Co}_\text{Fe}$  before and after 30,000 cycles. (E) Rotating ring-disk electrode (RRDE) measurements of  $\text{Zn}_6\text{Co}$  and  $\text{Zn}_6\text{Co}_\text{Fe}$  in 0.1M NaOH toward ORR. Ring and disk currents obtained at 1600 rpm and 5 mV/s. (F) Calculated electron transfer number and peroxide yield.

Stability was assessed for carbon nanocomposites derived from both  $\text{Zn}_6\text{Co}$  and  $\text{Zn}_6\text{Co}_\text{Fe}$  in an Ar-saturated 0.1M NaOH solution at a scan rate of 100 mV/s for 30,000 cycles (Figure 3D), where the carbon derived from  $\text{Zn}_6\text{Co}_\text{Fe}$  proved extraordinarily stable. After 30,000 CV cycles, there was virtually no loss in the potential region between 0.8 to 1.0 V, and the electrocatalytic activity still outperformed that of  $\text{Zn}_6\text{Co}$  carbon. To better evaluate the selectivity of the oxygen reduction process, the rotating ring-disk electrode (RRDE) method was employed to measure the peroxide yield, corresponding to the undesirable  $2\text{e}^-$  process. Figure 3E presents the ring and disk currents obtained for  $\text{Zn}_6\text{Co}$  and  $\text{Zn}_6\text{Co}_\text{Fe}$ .  $\text{Zn}_6\text{Co}_\text{Fe}$  exhibited a higher disk current, while its ring current decreased by 30%, when compared to  $\text{Zn}_6\text{Co}$ , suggesting a dominant four-electron transfer reaction. The electron transfer number (n) and peroxide yield values are presented in Figure 3F. For the  $\text{Zn}_6\text{Co}_\text{Fe}$  carbon, the n-value was determined to be above 3.9 over the potential region between 0.2 V to 0.9 V, and the generated peroxide was below 7%; a value that is about half, when compared to the 12%  $\text{H}_2\text{O}_2$  generation from  $\text{Zn}_6\text{Co}$ . The peroxide yield is relatively low when compared to other reported values in the literature. Our results are, in fact, comparable to other state-of-the-art catalysts. To make a better comparison, we have prepared a table that summarizes the peroxide yield of various materials in table S1 28-30, 47-55. Lowering down the peroxide yield would be most beneficial since it is well understood that peroxide can diffuse into the membrane and chemically break down to hydroxyl radicals. These radicals, in return, will react with perfluorosulfonic ionomers in the electrode and the membrane to produce hydrofluoric acid HF leading to the degradation of the MEA<sup>56</sup>. To address the disadvantage from produced peroxide, it requires collaborative efforts, also from the design of peroxide-tolerant membranes<sup>57</sup>.

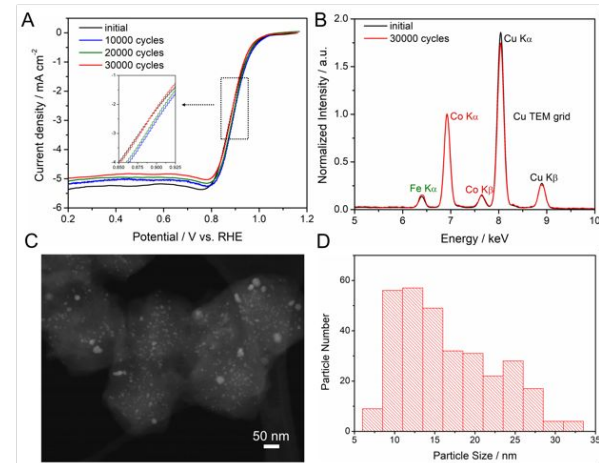


Figure 4. Degradation mechanism investigation of BMOF electrocatalysts during durability tests. (A) ORR polarization profiles of BMOF electrocatalysts at 1600 rpm and 5 mV/s after 10,000, 20,000 and 30,000 potential cycles from 0.6 to 1.0 V at 100 mV/s. (B) EDX spectra of BMOF at the initial state and after 30,000 cycles, showing a relatively stable Fe/Co atomic ratio. (C) STEM image of BMOF after 30,000 cycles, showing a majority of

1 small particles as well as aggregated larger particles. (D) PSD  
2 histogram of BMOF after 30,000 cycles, analyzed from (C) and  
3 Figure S8, showing an increasing number of larger particles,  
4 relative to the initial state in Figure 3B.

5 In order to implement Pt-free cathodes for industrial applications  
6 in alkaline membrane exchange fuel cells (AMEFCs), non-precious  
7 ORR electrocatalysts need to not only satisfy the requirements of  
8 high initial ORR activity, but also address long-term durability  
9 concerns.<sup>38</sup> The durability and the possible degradation  
10 mechanisms of ORR electrocatalysts need to not only satisfy the  
11 requirements of the BMOF electrocatalysts were investigated using  
12 STEM imaging and quantitative EDX analysis. As shown in Figure  
13 4A, the halfwave potentials of BMOF electrocatalysts shifted  
14 slightly positively after 10,000 and 20,000 cycles, indicating an  
15 initial catalyst activation. After 30,000 cycles, the  $E_{1/2}$  shifted in the  
16 negative direction by less than 5 mV, indicating a remarkable  
17 activity retention. The continuous decrease in  $I_d$  from -5.4 to -5.0  
18 mA/cm<sup>2</sup>, suggests a loss of electrochemical surface area (ECSA).  
19 EDX quantitative analysis and STEM images were employed to  
20 investigate the changes in microstructures and local chemical  
21 composition. EDX spectra of BMOF electrocatalysts, at the initial  
22 state and after 30,000 cycles, were normalized to the Co K $\alpha$  edge  
23 (783 eV) and showed little, if any, changes in the Fe K $\alpha$  edge (712  
24 eV). (Figure 4B) Quantitative analysis suggested that the relative  
25 contents of Co, and Fe changed from 89.2% and 10.8% ( $\pm$  0.6%) at  
26 the initial state to 88.5% and 11.5% ( $\pm$  0.8%) after 30,000 cycles,  
27 respectively. Given the relative error of EDX measurements, no  
28 significant changes in composition ratio was detected. STEM  
29 images of BMOF electrocatalysts after 30,000 cycles showed that  
30 the majority of the small particles were able to remain embedded  
31 in the carbon matrix with only a few aggregated larger particles  
32 evident. (Figure 4C). Around 300 Co<sub>0.9</sub>Fe<sub>0.1</sub> nanoparticles in  
33 Figures 4C and S11 were analyzed to form the particle size  
34 distribution (PSD) histogram in Figure 4D. It suggests that  
35 Co<sub>0.9</sub>Fe<sub>0.1</sub> NPs have a larger average particle size of 10-15 nm and  
36 a broader PSD after 30,000 cycles, when compared to the initial  
37 state in Figure 2, which may partially explain the decrease in  $I_d$  in  
38 Figure 4A. Initially, nearly all O<sub>2</sub> could be fully reduced to H<sub>2</sub>O via  
39 either the direct 4-electron transfer reaction or in a two-step process  
40 in which the generated peroxide is fully reduced (to water) by  
41 nearby sites before escaping the catalyst layer. After potential  
42 cycling process, some of active sites dissolved so that their density  
43 is lower. In this case, the peroxide has a higher possibility of  
44 diffusing into the bulk electrolyte causing a decrease in the limiting  
45 current. The  $E_{1/2}$  does not shift too much, in the kinetic-diffusion  
46 region, indicating that the kinetics is relatively fast. In summary,  
47 the excellent durability of BMOF derived electrocatalysts after  
48 30,000 cycles was ascribed to their capability to maintain a stable  
49 local chemical composition as well as a reasonably small particle  
50 size, highlighting the close interactions between Co<sub>0.9</sub>Fe<sub>0.1</sub> NPs and  
51 the MOF-derived carbon matrix. Here, we attributed the stability of  
52 our Co-Fe BMOF catalysts to the highly porous structure arising  
53 from the use of Zn as a sacrificial template in the reducing  
54 atmosphere and to the *in-situ* formation of the Co-Fe bimetallic  
55 nanoparticles. The annealing processes was deliberately conducted  
56 at H<sub>2</sub> flowing rates, known to promote the formation of carbon  
57 nanotubes on the surface of transition metals, like Co and Fe in this  
58 case, that help immobilize active sites. At the same time, Co and Fe  
59 are reduced and alloyed at the elevated temperatures employed  
60 during the formation of these CNTs and are subsequently wrapped  
in these tubes. In addition, the 1,2-imidazole ligands in the  
BMOF precursors bring N dopants in the carbon structure, which  
are able to not only provide additional catalytic pathways, but also  
bind and coordinate the metallic nanoparticles thus enhancing  
stability from both chemical and physical prospective. The porous

structure of our materials is maintained after extensive cycling, as  
evidenced by TEM. Together with the minimal compositional  
difference between a fresh sample and a sample after 30k cycles, it  
is reasonable to expect that the excellent stability derives from the  
structural and chemical integrity.

In addition, based on the Pourbaix diagram, the surface of the  
bimetallic Co-Fe nanoparticle is highly likely to be partially  
oxidized, in the form of Co and Fe oxide/hydroxide. It is  
possible/likely that, under working conditions (applied potential),  
there is a mixture of Co(OH)<sub>2</sub> and Co(OH)<sub>3</sub> (or Co<sub>2</sub>O<sub>3</sub>, Co<sub>3</sub>O<sub>4</sub> and  
CoO) for Co on the surface. Similarly, Fe likely exists as a mixture  
of Fe(OH)<sub>2</sub> and Fe(OH)<sub>3</sub> (or Fe<sub>2</sub>O<sub>3</sub> and Fe<sub>3</sub>O<sub>4</sub>). The average  
valence state is likely to be potential dependent; closer to +3 in the  
higher potential region (near 1V vs RHE) and near +2 when the  
applied potential is lower (near 0V vs RHE). Those two metals on  
the surface, simultaneously and synergistically catalyze the ORR  
reaction efficiently and stably.

## Conclusions

In summary, we have designed a family of BMOF derived Co-  
Fe alloys embedded in a carbon nanocomposite through the  
combination of the conventional self-assembly of MOFs and a  
guest-host strategy. Zn<sub>6</sub>Co proved to be the compositionally-  
optimized template and substrate, for the encapsulation of exterior  
Fe to generate the bimetallic nanoparticles-carbon composite. This  
nanocomposite, composed of porous carbon with high surface area  
and uniform distribution of Co<sub>0.9</sub>Fe<sub>0.1</sub> bimetallic nanoparticles,  
exhibited superior electrocatalytic activity towards the ORR, as  
well as robust stability after 30,000 cycles, owing to its structural  
and compositional integrity, as confirmed by STEM and EDX  
measurement. The synthesis strategy and optimization process  
presented here may provide with new pathways to push forward the  
substitution of Pt with more cost-effective electrocatalysts for fuel  
cell applications.

## ASSOCIATED CONTENT

### Supporting Information

The Supporting Information is available free of charge on the  
ACS Publications website.

Synthesis, structural characterizations of XRD, BET, SEM and  
TEM are available in the online version of the paper, including  
Figures S1-S11 (PDF)

## AUTHOR INFORMATION

### Corresponding Authors:

\*[hda1@cornell.edu](mailto:hda1@cornell.edu)

### Notes

The authors declare no competing financial interests.

Author Contributions:

<sup>†</sup> Y. X. and Y. Y. contributed equally to this work.

## Acknowledgements

This work was supported by the Center for Alkaline-Based  
Energy Solutions (CABES) and the Center for Energy Materials at  
Cornell (emc<sup>2</sup>), part of the Energy Frontier Research Center  
(EFRC) program supported by the U.S. Department of Energy,  
under grant DE-SC-0019445. Y. X. has synthesized the  
electrocatalyst and performed the electrochemical characterization.  
Y. Y. has performed TEM characterizations. Y. X. and Y. Y. are  
funded by DOE under the grant DE-SC-0019445. This work made  
use of TEM facilities at the Cornell Center for Materials Research  
(CCMR) which are supported through the National Science

Foundation Materials Research Science and Engineering Center (NSF MRSEC) program (DMR-1719875). We are grateful to Malcolm (Mick) Thomas at CCMR for the help in Nion UltraSTEM.

## REFERENCES

- Chu, S.; Majumdar, A. *Nature* **2012**, 488, 294.
- Xiong, Y.; Yang, Y.; Joress, H.; Padgett, E.; Gupta, U.; Yarlagadda, V.; Agyeman-Budu, D.; Huang, X.; Moylan, T. E.; Zeng, R.; Kongkanand, A.; Escobedo, F. A.; Brock, J. D.; DiSalvo, F. J.; Muller, D. A.; Abruña, H. D. *Proc. Natl. Acad. Sci. U.S.A.* **2019**, 116, 1974.
- Dresselhaus, M.; Thomas, I. *Nature* **2001**, 414, 332.
- Dunn, B.; Kamath, H.; Tarascon, J. *Science* **2001**, 334, 928.
- Kongkanand, A.; Mathias, M. *J. Phys. Chem. Lett.* **2016**, 7, 1127.
- Xiong, Y.; Yang, Y.; DiSalvo, F. J.; Abruña, H. D. *J. Am. Chem. Soc.* **2018**, 140, 7248.
- Xiong, Y.; Xiao, L.; Yang, Y.; DiSalvo, F. J.; Abruña, H. D. *Chem. Mater.* **2018**, 30, 1532.
- Meier, J.; Katsounaros, I.; Galeano, C.; Bongard, H.; Topalov, A.; Kostka, A.; Karschin, A.; Schüth, F.; Mayrhofer, K. *Energy Environ. Sci.* **2012**, 5, 9319.
- Liu, X.; Park, M.; Kim, M.; Gupta, S.; Wu, G.; Cho, J. *Angew. Chem. Int. Ed.* **2015**, 54, 9654.
- Wang, Y.; Qiao, J.; Baker, R.; Zhang, J. *Chem. Soc. Rev.* **2013**, 42, 5768.
- Yang, Y.; Wang, Y.; Xiong, Y.; Huang, X.; Shen, L.; Huang, R.; Wang, H.; Pastore, J. P.; Yu, S.-H.; Xiao, L.; Brock, J. D.; Zhuang, L.; Abruña, H. D. *J. Am. Chem. Soc.* **2019**, 141, 1463.
- Xiong, Y.; Yang, Y.; Feng, X.; DiSalvo, F. J.; Abruña, H. D. *J. Am. Chem. Soc.* **2019**, 141, 10, 4412.
- Wang, J.; Cui, W.; Liu, Q.; Xing, Z.; Asiri, A.; Sun, X. *Adv. Mater.* **2015**, 28, 215.
- Zhu, Y.; Ma, T.; Jaroniec, M.; Qiao, S. *Angew. Chem. Int. Ed.* **2016**, 55, 215.
- Cheng, F.; Shen, J.; Peng, B.; Pan, Y.; Tao, Z.; Chen, J. *Nat. Chem.* **2010**, 3, 79.
- Jiao, F.; Frei, H. *Angew. Chem. Int. Ed.* **2009**, 48, 1841.
- Yeo, B.; Bell, A. *J. Am. Chem. Soc.* **2011**, 133, 5587.
- Li, T.; Xue, B.; Wang, B.; Guo, G.; Han, D.; Yan, Y.; Dong, A. *J. Am. Chem. Soc.* **2017**, 139, 12133.
- Ren, H.; Wang, Y.; Yang, Y.; Tang, X.; Peng, Y.; Peng, H.; Xiao, L.; Lu, J.; Abruña, H. D.; Zhuang, L. *ACS Catal.* **2017**, 7, 6485.
- Gong, K.; Du, F.; Xia, Z.; Durstock, M.; Dai, L. *Science* **2009**, 323, 760.
- Liang, H.; Wei, W.; Wu, Z.; Feng, X.; Müllen, K.; *J. Am. Chem. Soc.* **2013** 135, 16002.
- Liang, Y.; Wang, H.; Zhou, J.; Li, Y.; Wang, J.; Regier, T.; Dai, H. *J. Am. Chem. Soc.* **2012**, 134, 3517.
- Suntivich, J.; Gasteiger, H.; Yabuuchi, N.; Nakanishi, H.; Goodenough, J.; Shao-Horn, Y. *Nat. Chem.* **2011**, 3, 546.
- Wu, G.; More, K.; Johnston, C.; Zelenay, P. *Science* **2011**, 332, 443.
- Chung, H.; Cullen, D.; Higgins, D.; Sneed, B.; Holby, E.; More, K.; Zelenay, P. *Science*, **2017**, 357, 479.
- Proietti, E.; Jaouen, F.; Lefèvre, M.; Larouche, N.; Tian, J.; Herranz, J.; Dodelet, J. *Nat. Commun.* **2011**, 2, 416.
- Lefèvre, M.; Proietti, E.; Jaouen, F.; Dodelet, J. *Science*, **2009**, 324, 71.
- Lu, Y.; Wang, L.; Preuß, K.; Qiao, M.; Titirici M.-M.; Varcoe, J.; Cai, Q. *J. Power Sources* **2017**, 372, 82.
- Peng, X.; Omasta, T.; Magliocca, E.; Wang, L.; Varcoe, J.; Mustain, W. *Angew. Chem.*, **2018**, 131, 1058.
- Sa, Y.; Seo, D.; Woo, J.; Lim, J.; Cheon, J.; Yang, S.; Lee, J.; Kang, D.; Shin, T.; Shin, H.; Jeong, H.; Kim, C.; Kim, M.; Kim, T.; Joo, S.; *J. Am. Chem. Soc.* **2016**, 138, 15046.
- Venna, S.; Jasinski, J.; Carreon, M. *J. Am. Chem. Soc.* **2010**, 132, 18030.
- Banerjee, R.; Phan, A.; Wang, B.; Knobler, C.; Furukawa, H.; O'Keeffe, M.; Yaghi, O. *Science* **2008**, 319, 939.
- Tang, J.; Salunkhe, R.; Liu, J.; Torad, N.; Imura, M.; Furukawa, S.; Yamauchi, Y. *J. Am. Chem. Soc.* **2015**, 137, 1572.
- Li, Y.; Jia, B.; Fan, Y.; Zhu, K.; Li, G.; Su, C. *Adv. Energy Mater.* **2017**, 8, 1702048.
- Furukawa, H.; Cordova, K. E.; O'Keeffe, M.; Yaghi, O. M. *Science* **2013**, 341, 1230444.
- Zhao, Y.; Yang, L.; Chen, S.; Wang, X.; Ma, Y.; Wu, Q.; Jiang, Y.; Qian, W.; Hu, Z. *J. Am. Chem. Soc.* **2013**, 135, 1201.
- Sharifi, T.; Hu, G.; Jia, X.; Wågberg, T. *ACS Nano* **2012**, 6, 8904.
- Xia, B.; Yan, Y.; Li, N.; Wu, H.; Lou, X.; Wang, X. *Nat. Energy* **2016**, 1, 15006.
- Wu, M.; Wang, K.; Yi, M.; Tong, Y.; Wang, Y.; Song, S. *ACS Catal.* **2017**, 7, 6082.
- Chen, Y.; Wang, C.; Wu, Z.; Xiong, Y.; Xu, Q.; Yu, S.; Jiang, H. *Adv. Mater.* **2015**, 27, 5010.
- Li, Y.; Jia, B.; Fan, Y.; Zhu, K.; Li, G.; Su, C. *Adv. Energy Mater.* **2017**, 8, 1702048.
- Behr, M.; Gaulding, E.; Mkhoyan, K.; Aydil, E. *J. Appl. Phys.* **2010**, 108, 053303.
- Park, K.; Ni, Z.; Cote, A.; Choi, J.; Huang, R.; Uribe-Romo, F.; Chae, H.; O'Keeffe, M.; Yaghi, O. *Proc. Natl. Acad. Sci.* **2006**, 103, 10186.
- Huang, X.; Lin, Y.; Zhang, J.; Chen, X. *Angew. Chem. Int. Ed.* **2006**, 45, 1557.
- Meng, F.; Wang, Z.; Zhong, H.; Wang, J.; Yan, J.; Zhang, X. *Adv. Mater.* **2016**, 28, 7948.
- Cliff, G.; Lorimer, G. *J. Microsc.* **1975**, 103, 203.
- Singh, S.; Kashyap, V.; Manna, N.; Bhange, S.; Soni, R.; Boukerroub, R.; Szunerits, S.; Kurungot, S. *ACS Catal.* **2017**, 7, 6700.
- Fu, G.; Yan, X.; Chen, Y.; Xu, L.; Sun, D.; Lee, J.; Tang, Y. *Adv. Mater.* **2018**, 30, 1704609.
- Wu, M.; Wang, K.; Yi, M.; Tong, Y.; Wang, Y.; Song, S. *ACS Catal.* **2017**, 7, 6082.
- Wang, Y.; Yang, Y.; Jia, S.; Wang, X.; Lyu, K.; Peng, Y.; Zheng, H.; Wei, X.; Ren, H.; Xiao, L.; Wang, J.; Muller, D.; Abruña, H.; Hwang, B.; Lu, J.; Zhuang, L. *Nat. Comm.* **2019**, 10.
- Sun, J.; Lowe, S.; Zhang, L.; Wang, Y.; Pang, K.; Wang, Y.; Zhong, Y.; Liu, P.; Zhao, K.; Tang, Z.; Zhao, H. *Angew. Chem. Int. Ed.* **2018**, 130, 16749.
- Wang, J.; Liu, W.; Luo, G.; Li, Z.; Zhao, C.; Zhang, H.; Zhu, M.; Xu, Q.; Wang, X.; Zhao, C.; Qu, Y.; Yang, Z.; Yao, T.; Li, Y.; Lin, Y.; Wu, Y.; Li, Y. *Energy Environ. Sci.* **2018**, 11, 3375.
- Li, S.; Cheng, C.; Liang, H.; Feng, X.; Thomas, A. *Adv. Mat.* **2017**, 29, 1700707.
- Hu, C.; Dai, L. *Adv. Mat.* **2016**, 29, 1604942.
- Xiang, Z.; Xue, Y.; Cao, D.; Huang, L.; Chen, J.; Dai, L. *Angew. Chem. Int. Ed.* **2014**, 126, 2465.
- Sethuraman, V.; Weidner, J.; Haug, A.; Motupally, S.; Protsailo, L. *J. Electrochem. Soc.* **2008**, 155, B50.
- Kim, Y.; Moh, L.; Swager, T. *ACS Appl. Mater. Interfaces* **2017**, 9, 42409.
- Gasteiger, H.; Kocha, S.; Sompalli, B.; Wagner, F. *Appl. Catal. B*, **2005**, 56, 9.

## TOC graphic

